NEW LINEAR TRANSFORMS FOR DATA ON A FOURIER 2-SPHERE WITH APPLICATION TO DIFFUSION MRI

Justin P. Haldar and Richard M. Leahy

Signal and Image Processing Institute, Brain and Creativity Institute, and Dornsife Cognitive Neuroscience Imaging Center, University of Southern California, Los Angeles, CA 90089

ABSTRACT

This paper describes a new family of linear transforms for data restricted to the surface of a 2-sphere in three-dimensional Fourier space. These transforms generalize the existing Funk-Radon Transform, which has previously been used with great success to extract microstructural tissue orientation information from high angular resolution magnetic resonance diffusion imaging data. Several properties of the new transforms are described, and computationally efficient implementations are derived using spherical harmonic basis functions. A special case from this family, called the Funk-Radon and Cosine Transform, is introduced and evaluated. The method is illustrated with simulated and real diffusion weighted MRI data.

Index Terms— Diffusion Magnetic Resonance Imaging, Funk-Radon and Cosine Transform, Orientation Distribution Functions, q-Space

1. INTRODUCTION

We assume an inverse problem scenario where an unknown real-valued symmetric function $f(\mathbf{x}) \in \mathcal{L}_1\left(\mathbb{R}^3\right)$ is observed through the values of its three-dimensional Fourier transform

$$E(\mathbf{q}) = \int_{\mathbb{R}^3} f(\mathbf{x}) \exp\left(-i2\pi\mathbf{q}^T\mathbf{x}\right) d\mathbf{x}. \tag{1}$$

$E(\mathbf{q})$ is only observed at points $\mathbf{q} \in \mathcal{S}_\rho^2$, where $\mathcal{S}_\rho^2 = \left\{\mathbf{q} \in \mathbb{R}^3 : \|\mathbf{q}\|_{\ell_2} = \rho\right\}$ is the 2-sphere of radius ρ. This kind of spherical Fourier sampling is an accurate model of the data acquisition procedure in high angular resolution magnetic resonance diffusion imaging (HARDI), where $f(\mathbf{x})$ is a probability distribution that represents molecular diffusion characteristics within an imaging voxel. Diffusion information provides insight into the structure and connectivity of anisotropic structures like brain white matter fibers.

In this work, we consider the general family of linear transforms R_G that map this kind of data onto $\mathcal{S}_1^2$ according to

$$R_G\left\{E(\mathbf{q})\right\}(\mathbf{u}) = \int_{\mathbf{q}\in\mathcal{S}_\rho^2} E(\mathbf{q})\, G\left(\mathbf{u}^T\mathbf{q}\right) d\mathbf{q}, \tag{2}$$

where $\mathbf{u} \in \mathcal{S}_1^2$ and $G(t)$ is a transform kernel. A special case of (2), known as the Funk-Radon Transform (FRT), has been previously proposed by Tuch *et al.* in this context [1]. The FRT used $G\left(\mathbf{u}^T\mathbf{q}\right) = \delta\left(\mathbf{u}^T\mathbf{q}\right)$, where $\delta(\cdot)$ denotes the Dirac delta function. In this notation, the delta function is being used to define a contour integral around the equator of $\mathcal{S}_\rho^2$ that is perpendicular to $\mathbf{u}$. The FRT is useful for HARDI data because it can be used to approximate the q-ball imaging (QBI) orientation distribution function (ODF)

$$\begin{aligned} ODF_{\mathrm{QBI}}(\mathbf{u}) &= \int_{-\infty}^{\infty} f(\alpha\mathbf{u})\, d\alpha \\ &= \int_{-\infty}^{\infty} \tilde{f}_{\mathbf{u}}(0,0,z)\, dz, \end{aligned} \tag{3}$$

which provides important information for inferring white matter fiber orientations in the brain. Throughout this work, we will use the notation that for any function $s(\mathbf{x})$, $\tilde{s}_{\mathbf{u}}(\mathbf{x})$ represents a rotated version of $s(\mathbf{x})$ such that the $\mathbf{u}$ vector is aligned with the z-axis of $\tilde{s}_{\mathbf{u}}(\mathbf{x})$.

While many alternative approaches have been proposed to estimate orientation information from HARDI data (see [2] and its references), the FRT has a unique combination of useful characteristics: it does not require a strict parametric model of the diffusion signal, it is linear and its theoretical characteristics can be evaluated analytically, and it can be computed very quickly using efficient algorithms [3, 4]. Despite this, a significant disadvantage has been that FRT-based orientation estimates can have lower resolution/accuracy relative to some of the alternative processing methods (e.g., [5–7]), partly due to the fact that the approach is based on a sub-optimal definition of the ODF [7]. A better choice of ODF is [7]

$$\begin{aligned} ODF(\mathbf{u}) &= \int_{-\infty}^{\infty} f(\alpha\mathbf{u})\, \alpha^2 d\alpha \\ &= \int_{-\infty}^{\infty} \tilde{f}_{\mathbf{u}}(0,0,z)\, z^2 dz, \end{aligned} \tag{4}$$

This work was supported in part by the following research grants: NIH-P41-RR013642, NIH-R01-EB000473, NIH-R01-NS074980, and NIH-P50-NS019632.

which includes the appropriate volume normalization for radial integration in spherical coordinates, and ensures that the ODF is a valid marginal distribution when $f(\mathbf{x})$ is a valid probability distribution. To the best of our knowledge, no linear transforms have been proposed to approximate (4) from HARDI data.

In this work, we establish the characteristics of the class of linear transforms that can be achieved by (2). In addition, we introduce a new transform from this class, called the Funk-Radon and Cosine Transform (FRACT), which we show can be used to accurately approximate (4). Results are demonstrated in the context of experimental HARDI data.

2. LINEAR TRANSFORMS OF THE FOURIER 2-SPHERE

It is well known that the Fourier transforms of $\mathcal{L}_1\left(\mathbb{R}^3\right)$ functions are bounded and uniformly continuous. Consequently, the linear transform in (2) will always be well defined for any transform kernel satisfying $G\left(\mathbf{u}^T\cdot\right) \in \mathcal{L}_1\left(\mathcal{S}^2_\rho\right)$, which happens if and only if $G(t) \in \mathcal{L}_1([-\rho,\rho])$.

To begin our discussion, we first note that for any $G\left(\mathbf{u}^T\cdot\right) \in \mathcal{L}_1\left(\mathcal{S}^2_\rho\right)$, we can express the action of (2) applied to noiseless data as

$$\begin{aligned} &R_G\left\{E(\mathbf{q})\right\}(\mathbf{u}) \\ &= \int_{\mathbf{q}\in\mathcal{S}^2_\rho}\left(\int_{\mathbb{R}^3} f(\mathbf{x})\exp\left(-i2\pi\mathbf{q}^T\mathbf{x}\right)d\mathbf{x}\right)G\left(\mathbf{u}^T\mathbf{q}\right)d\mathbf{q} \\ &= \int_{\mathbb{R}^3} f(\mathbf{x})\left(\int_{\mathbf{q}\in\mathcal{S}^2_\rho} G\left(\mathbf{u}^T\mathbf{q}\right)\exp\left(-i2\pi\mathbf{q}^T\mathbf{x}\right)d\mathbf{q}\right)d\mathbf{x} \\ &= \int_{\mathbb{R}^3} f(\mathbf{x})\, g(\mathbf{u},\mathbf{x})\, d\mathbf{x}, \end{aligned} \tag{5}$$

where we have introduced

$$g(\mathbf{u},\mathbf{x}) \equiv \int_{\mathbf{q}\in\mathcal{S}^2_\rho} G\left(\mathbf{u}^T\mathbf{q}\right)\exp\left(-i2\pi\mathbf{q}^T\mathbf{x}\right)d\mathbf{q}. \tag{6}$$

The function $g(\mathbf{u},\mathbf{x})$ can be interpreted much like a point-spread function, and through (5), describes how the transformed data relates to the unobserved signal of interest $f(\mathbf{x})$. By manipulating the integrals, (6) can also be expressed in rotated coordinates as

$$\tilde{g}_{\mathbf{u}}(x,y,z) = \int_{-\rho}^{\rho} G(\tau)\, B(x,y,\tau)\exp(-i2\pi\tau z)\, d\tau, \tag{7}$$

with

$$B(x,y,\tau) = 2\pi\rho J_0\left(2\pi\sqrt{\rho^2-\tau^2}\sqrt{x^2+y^2}\right). \tag{8}$$

As can be seen from (7) and (8), any response function $g(\mathbf{u},\mathbf{x})$ resulting from (2) can be expressed as a linear combination of Bessel functions modulated by complex exponentials and possesses axial symmetry about the z-axis. Since $f(\mathbf{x})$ is real-valued and symmetric, we can further restrict attention to functions $g(\mathbf{u},\mathbf{x})$ that are also real-valued and symmetric with respect to $\mathbf{x}$. In turn, this restricts attention to real-valued and symmetric kernel functions $G(\cdot)$, so that all of the interesting $g(\mathbf{u},\mathbf{x})$ that can be obtained with (2) can equivalently be expressed as linear combinations of cosine-modulated Bessel functions.

2.1. Fast Computation

The previous subsection described the class of interesting transforms that can be obtained from (2). In this subsection, we will show that the computation of this transform can be performed easily by making using of spherical harmonics. The spherical harmonics form an orthonormal basis for $\mathcal{S}^2_1$, and are frequently defined as [3]

$$Y^m_\ell(\mathbf{u}) = \sqrt{\frac{2\ell+1}{4\pi}\frac{(\ell-m)!}{(\ell+m)!}}P^m_\ell(\cos\theta)\exp(im\phi), \tag{9}$$

where the harmonic degree $\ell = 0,1,\ldots,\infty$, and the harmonic order $m = -\ell,\ldots,0,\ldots,\ell$. In this expression, $\theta \in [0,\pi]$ is the polar angle and $\phi \in [0,2\pi]$ is the azimuthal angle for the vector $\mathbf{u}$, and $P^m_\ell(\cdot)$ is the associated Legendre function of degree ℓ and order m.

Use of spherical harmonic representations is common in the HARDI literature, partly due to the observation that the spherical harmonics are eigenfunctions of the FRT [3, 4]. Thus, if $E(\mathbf{q})$ is represented through its coefficients $\{c_{\ell m}\}$ in the spherical harmonic basis as

$$E(\mathbf{q}) = \sum_{\ell=0}^{\infty}\sum_{m=-\ell}^{\ell} c_{\ell m}Y^m_\ell(\mathbf{q}), \tag{10}$$

then we can efficiently compute the FRT through simple rescaling of each spherical harmonic coefficient by the corresponding eigenvalue. While there are several methods of deriving the eigenfunction relationship for the FRT, Descoteaux *et al.* [3] used the Funk-Hecke theorem as the basis for their derivations.

In this work, we note that the Funk-Hecke theorem also shows that the spherical harmonics are eigenfunctions for most choices of transform kernels $G(t)$:

Theorem (Funk-Hecke, adapted from [8]): *Suppose that $G(t) \in \mathcal{L}_1([-\rho,\rho])$. Then for any $\mathbf{u} \in \mathcal{S}^2_1$,*

$$\int_{\mathbf{q}\in\mathcal{S}^2_\rho} G\left(\mathbf{u}^T\mathbf{q}\right)Y^m_\ell(\mathbf{q})\, d\mathbf{q} = \lambda^G_\ell Y^m_\ell(\mathbf{u}), \tag{11}$$

where the eigenvalue λ^G_ℓ is given by

$$\lambda^G_\ell = 2\pi\rho^2\int_{-1}^{1} P_\ell(t)\, G(\rho t)\, dt. \tag{12}$$

$P_\ell(t)$ in (12) *is the Legendre polynomial of degree ℓ.*

As a result of this theorem, (2) can be expressed for $G(t) \in \mathcal{L}_1([-\rho,\rho])$ in terms of $\{c_{\ell m}\}$ as

$$R_G\{E(\mathbf{q})\}(\mathbf{u}) = \sum_{\ell=0}^{\infty} \lambda_\ell^G \sum_{m=-\ell}^{\ell} c_{\ell m} Y_\ell^m(\mathbf{u}). \quad (13)$$

While $G(t) = \delta(t-\xi) \notin \mathcal{L}_1([-\rho,\rho])$, the eigenfunction relationship still applies for the contour integrals implied by transform kernels of this form. In particular, the corresponding eigenvalues for this case are

$$\lambda_\ell^G = 2\pi\rho P_\ell(\xi/\rho). \quad (14)$$

3. THE FUNK-RADON AND COSINE TRANSFORM

Based on the family of transforms described in the previous section, we propose the FRACT, which we define by the transform kernel

$$G(t) = \frac{1}{8\pi^3\xi^2\rho}\left(2\delta(t) - \delta(t+\xi) - \delta(t-\xi)\right), \quad (15)$$

for some ξ with $0 < \xi < \rho$. This definition implies that the FRACT has

$$\begin{aligned}\tilde{g}_{\mathbf{u}}(x,y,z) = &\\ &\frac{1}{2\pi^2\xi^2} J_0\left(2\pi\rho\sqrt{x^2+y^2}\right)\\ &- \frac{1}{2\pi^2\xi^2} J_0\left(2\pi\sqrt{\rho^2-\xi^2}\sqrt{x^2+y^2}\right)\cos(2\pi\xi z),\end{aligned} \quad (16)$$

and has spherical harmonic eigenvalues given by

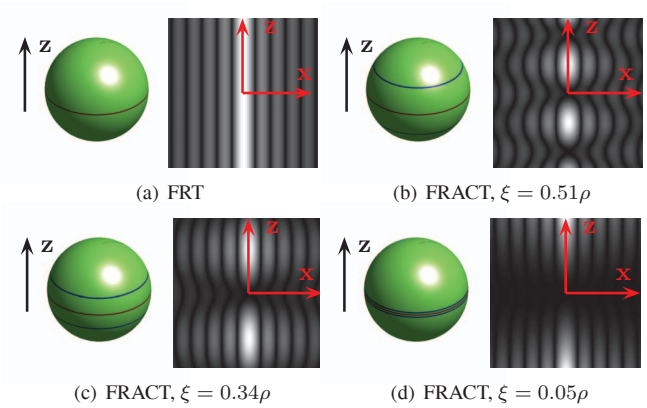
$$\lambda_\ell^G = \frac{1}{4\pi^2\xi^2}\left(2P_\ell(0) - P_\ell(\xi/\rho) - P_\ell(-\xi/\rho)\right). \quad (17)$$

An important characteristic of the FRACT is the behavior of $\tilde{g}_{\mathbf{u}}(0,0,z)$ as a function of z. In particular, for small values of ξz, FRACT satisfies

$$\begin{aligned}\tilde{g}_{\mathbf{u}}(0,0,z) &= \frac{1}{2\pi^2\xi^2}\left(1-\cos(2\pi\xi z)\right)\\ &\approx z^2,\end{aligned} \quad (18)$$

where the approximation is obtained by neglecting the higher-order terms in the Taylor series expansion of the cosine. As a result, the FRACT can be used to compute an approximation of the ODF defined in (4).

For a given ρ, the FRACT has a single parameter ξ that controls its behavior, and examples of $G(\mathbf{u}^T\mathbf{q})$ and $\tilde{g}_{\mathbf{u}}(x,y,z)$ for different choices of ξ are illustrated in Fig. 1. For comparison, the standard FRT is also shown. As can be seen, the ability of the FRACT to approximate z^2 improves as ξ decreases towards 0. However, it should also be noted that as ξ decreases towards 0, the energy of $\tilde{g}_{\mathbf{u}}(\mathbf{x})$ is being distributed further and further from the origin. Since the functions $f(\mathbf{x})$ encountered in diffusion MRI typically have concentrated signal energy at the origin, the signal-to-noise ratio for the FRACT will also diminishes as ξ decreases. However, the value of $f(\mathbf{x})$ in the region farther from the origin will typically provide more information regarding oriented anisotropic diffusion. For comparison, note that the signal from the FRT will generally be dominated by the region of $f(\mathbf{x})$ near the origin. As a result, the FRT would be expected to have higher SNR than the FRACT, but could be less sensitive to tissue orientation due to signal leakage from regions near the origin in the plane orthogonal to $\mathbf{u}$.



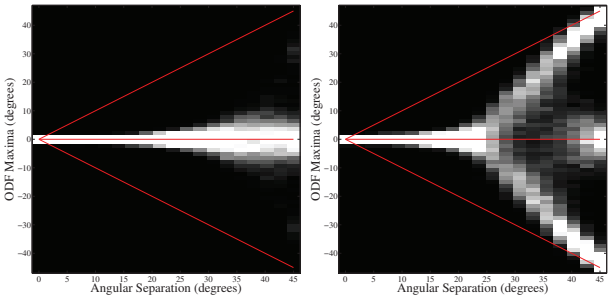
(a) FRT (b) FRACT, $\xi = 0.51\rho$ (c) FRACT, $\xi = 0.34\rho$ (d) FRACT, $\xi = 0.05\rho$

Fig. 1. Illustration of FRACT for different choices of ξ. In each subfigure, the left image shows $G(\mathbf{u}^T\mathbf{q})$ for $\mathbf{q}$ on the sphere, and the right image shows the magnitude of $\tilde{g}_{\mathbf{u}}(x,0,z)$ in the x-z plane, both for the case where $\mathbf{u}$ is oriented along the z-axis. Note that $\tilde{g}_{\mathbf{u}}(x,y,z)$ is rotationally symmetric about the z-axis.

4. EVALUATION

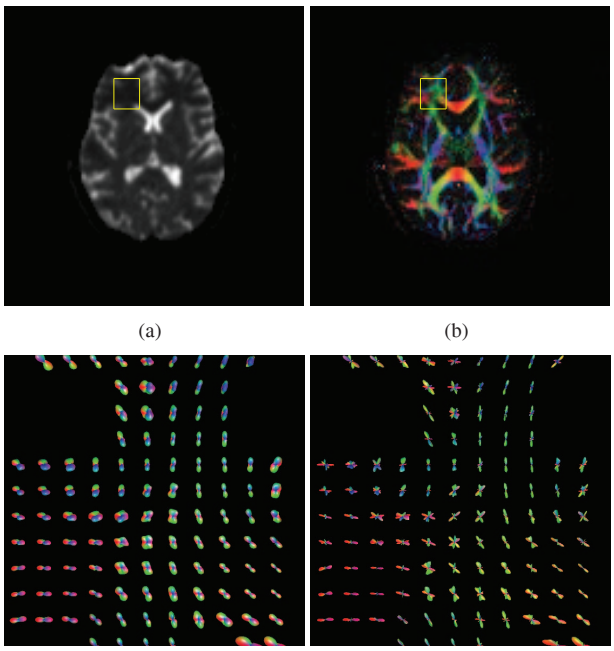
Based on the theoretical results presented in the previous sections, we expect that the FRACT could have significantly improved performance in resolving multiple orientations from HARDI data, potentially at the expense of an increased sensitivity to noise. We extensively tested the FRACT with simulated and real data, and confirmed that FRACT has significantly enhanced angular resolution than the FRT with a slightly higher variance. We show only a small set of these results here due to space constraints.

Figure 2 shows a simulated multi-fiber example in which the FRT and the FRACT are evaluated for a three-tensor diffusion model over a range of different angular separations between the tensors. Since the estimation of three distinct coplanar orientations can be very challenging, we show results for a high SNR case with a large b-value. As can be seen, the FRACT is quite successful at identifying and localizing the three different dominant orientations, while the FRT has limited ability to resolve multiple orientations from this data.



(a) FRT (b) FRACT

Fig. 2. Histograms for the locations of local maxima extracted from (a) FRT profiles and (b) FRACT profiles as a function of the true angular separation between three simulated tensors. 1000 trials were performed, and the gray scale is set to saturate at 100 counts in a single histogram bin for improved visualization. The true orientations of the three tensors are also indicated using red lines. These simulations used an SNR of 80 for the $b = 0$ s/mm^2 image and a b-value of 5000 s/mm^2 for diffusion encoding.



(a) (b)

(c) FRT (d) FRACT

Fig. 3. Application of the FRT and the FRACT to *in vivo* human brain data. (a) A $b = 0$ s/mm^2 image from a slice of interest. (b) The corresponding DTI fit, where image intensity corresponds to the fractional anisotropy of the tissue, while the image color corresponds to the orientation of the principal eigenvector of the estimated diffusion tensor. The yellow boxes in (a) and (b) indicate a region of interest (ROI) from the white matter core of the frontal lobe in which complicated fiber crossing patterns are known to occur. ODFs from the ROI are shown for (c) the FRT and (d) the FRACT.

Representative results with *in vivo* brain data, acquired at the USC Dornsife Cognitive Neuroscience Imaging Center (144 directions with $b = 2500$ s/mm^2), are shown in Fig. 3. ξ was manually set to 0.05ρ, based on bias/variance considerations. While there is no gold standard to compare to, these results are visually similar to our simulations, and suggest that the FRACT can offer significantly sharper ODF profiles than the FRT, enabling better identification of crossing fiber structure in regions of complicated tissue architecture.

5. CONCLUSION

This work introduced a new family of transforms for data sampled on the Fourier 2-sphere. Compared to existing methods for processing this kind of data, these transforms are linear, flexible, and can be computed efficiently. This work also introduced the FRACT for the processing of HARDI data. Compared to the existing FRT, FRACT has significant advantages in its ability to accurately resolve the angular orientation of anisotropic structures from DW-MRI data. These advantages were confirmed with simulations and real MR data. We expect that the proposed transforms will prove useful for future studies in this area.

6. REFERENCES

[1] D. S. Tuch, "Q-ball imaging," *Magn. Reson. Med.*, vol. 52, pp. 1358–1372, 2004.

[2] P. Fillard, M. Descoteaux, A. Goh, S. Gouttard, B. Jeurissen, J. Malcolm, A. Ramirez-Manzanares, M. Reisert, K. Sakaie, F. Tensaouti, T. Yo, J.-F. Mangin, and C. Poupon, "Quantitative evaluation of 10 tractography algorithms on a realistic diffusion MR phantom," *NeuroImage*, vol. 56, pp. 220–234, 2011.

[3] M. Descoteaux, E. Angelino, S. Fitzgibbons, and R. Deriche, "Regularized, fast, and robust analytical Q-ball imaging," *Magn. Reson. Med.*, vol. 58, pp. 497–510, 2007.

[4] E. Kaden and F. Kruggel, "A reproducing kernel Hilbert space approach for Q-ball imaging," *IEEE Trans. Med. Imag.*, vol. 30, pp. 1877–1886, 2011.

[5] J.-D. Tournier, C.-H. Yeh, F. Calamante, K.-H. Cho, A. Connelly, and C.-P. Lin, "Resolving crossing fibres using constrained spherical deconvolution: Validation using diffusion-weighted imaging phantom data," *NeuroImage*, vol. 42, pp. 617–625, 2008.

[6] A. Ramirez-Manzanares, M. Rivera, B. C. Vemuri, P. Carney, and T. Mareci, "Diffusion basis functions decomposition for estimating white matter intravoxel fiber geometry," *IEEE Trans. Med. Imag.*, vol. 26, pp. 1091–1102, 2007.

[7] I. Aganj, C. Lenglet, G. Sapiro, E. Yacoub, K. Ugurbil, and N. Harel, "Reconstruction of the orientation distribution function in single- and multiple-shell q-ball imaging within constant solid angle," *Magn. Reson. Med.*, vol. 64, pp. 554–566, 2010.

[8] W. Freeden and M. Schreiner, *Spherical Functions of Mathematical Geosciences: A Scalar, Vectorial, and Tensorial Setup*, ser. Advances in Geophysical and Environmental Mechanics and Mathematics. New York: Springer, 2009.